Geochemistry Geophysics Geosystems G3
AN ELECTRONIC JOURNAL OF THE EARTH SCIENCES
Published by AGU and the Geochemical Society

*Article*
Volume 6, Number 1
1 February 2005
Q02H16, doi:10.1029/2004GC000801
ISSN: 1525-2027

# Continuous geomagnetic field models for the past 7 millennia: 2. CALS7K

**M. Korte**
*GeoForschungsZentrum Potsdam, Telegrafenberg, 14473 Potsdam, Germany (monika@gfz-potsdam.de)*

**C. G. Constable**
*Institute for Geophysics and Planetary Physics, Scripps Institution of Oceanography, University of California, San Diego, 9500 Gilman Drive, La Jolla, California, 92093-0225, USA (cconstable@ucsd.edu)*

[1] We present two continuous global geomagnetic field models for recent millennia: CALS3K.2, covering the past 3000 years, and CALS7K.2, covering 7000 years from 5000 BC to 1950 AD. The models were determined by regularized least squares inversion of archeomagnetic and paleomagnetic data using spherical harmonics in space and cubic B splines in time. They are derived from a greatly increased number of paleomagnetic directional data, compared to previous efforts, and for the first time a significant amount of archeointensity data is used in this kind of global model, allowing the determination of evolution of geomagnetic dipole strength. While data accuracy and dating uncertainties remain a limitation, reliable low-resolution global models can be obtained. The results agree well with previous results from virtual axial dipole moment (VADM) studies from archeomagnetic intensity data apart from a systematic offset in strength. A comparison of model predictions with the previous 3000 year model, CALS3K.1, gives general agreement but also some significant differences particularly for the early epochs. The new models suggest that the prominent two northern hemisphere flux lobes are more stationary than CALS3K.1 implied, extending considerably the time span of stationary flux lobes observed in historical models. Between 5000 BC and 2000 BC there are time intervals of weak dipole moment where dipole power is exceeded by low-degree nondipole power at the core-mantle boundary. Model coefficients and evaluation code can be obtained from the EarthRef Digital Archive (ERDA) together with animations and snapshots plots for every 100 years at http://www.earthref.org. Detailed URLs for the different material are listed in Appendix A.

**Components:** 8941 words, 11 figures, 4 tables.

**Keywords:** Geomagnetic field models; archeomagnetism; lake sediments; paleointensity; geomagnetic dipole moment.

**Index Terms:** 1503 Geomagnetism and Paleomagnetism: Archeomagnetism; 1521 Geomagnetism and Paleomagnetism: Paleointensity; 1532 Geomagnetism and Paleomagnetism: Reference fields: regional, global.

**Received** 13 July 2004; **Revised** 27 October 2004; **Accepted** 29 November 2004; **Published** 1 February 2005.

Korte, M., and C. G. Constable (2005), Continuous geomagnetic field models for the past 7 millennia: 2. CALS7K, *Geochem. Geophys. Geosyst.*, *6*, Q02H16, doi:10.1029/2004GC000801.

**Theme:** Geomagnetic Field Behavior Over the Past 5 Myr
**Guest Editors:** Cathy Constable and Catherine Johnson

## 1. Introduction

[2] The evolution of the geomagnetic field prior to times of direct measurement is studied by analyzing remanent magnetization of archeological material, lava flows and lake sediments. The number of sufficiently accurately dated results from worldwide locations has become large enough to allow the development of continuous global models on the millennial timescale.

[3] Global models offer better insight into the field evolution and underlying processes at the core-mantle boundary (CMB) than individual time series. Moreover, they can help to verify the dating of individual results by assessing the regional consistency between different locations. Earlier attempts at global analyses for the past 2000 years came from *Braginskiy and Burlatskaya* [1979], *Sakai* [1980], *Ohno and Hamano* [1993], and *Hongre et al.* [1998], which all were based on low-degree spherical harmonic models. *Constable et al.* [2000] published global snapshot models in 100 year intervals covering the past 3000 years and based on a regularized spherical harmonic expansion up to degree and order 10 and a limited collection of paleomagnetic directional data. The same data set was used by *Korte and Constable* [2003] to develop a temporally continuous model for the time span 1000 BC to 1800 AD, named CALS3K.1 (Continuous Archeomagnetic and Lake Sediment model for the past 3k years, version 1). The data compilation consisted of 100 year interval directional results from 12 smoothed lake sediment records and 12 archeomagnetic composite curves, reduced to representative locations. To improve the data basis, a new global compilation has been set up by *Korte et al.* [2005], including also a significant number of archeomagnetic intensity data (A. Genevey et al., A new archeointensity database for the past 10 millennia, manuscript in preparation, 2005) and without a priori smoothing in time or reduction to certain average locations. On the basis of this hugely increased number of data we have developed new global models. With CALS3K.2 we present an improved model for the past 3000 years and with CALS7K.1 and CALS7K.2 the first continuous global models for the past 7000 years.

[4] CALS7K.1 was our first preferred model, but during the revision stage of this paper we noticed that we had not downweighted some of the sediment inclination data from Palmer Deep, Antarctic Peninsula (data from *Brachfeld et al.* [2000]), according to the very large uncertainty estimates that were given for some time spans by the original author [*Brachfeld et al.*, 2000; see also *Korte et al.*, 2005]. We corrected this, but decided to name our new preferred model CALS7K.2 and keep CALS7K.1 as a reference as we had already distributed that model to several colleagues. It is still available from the EarthRef Digital Archive (ERDA). Differences are marginal for the northern hemisphere and for those parts of the southern hemisphere away from the location of Palmer Deep, as we will discuss further in section 5.1.

[5] With CALS3K.1, assumptions had to be made about the field's axial dipole strength to compensate for the lack of intensity data. Until now, dipole strength evolution of past millennia has been estimated through the determination of virtual dipole moments (VDMs) and virtual axial dipole moments (VADMs) from archeomagnetic intensity data [*McElhinny and Senanayake*, 1982; *Yang et al.*, 2000]. Individual results are biased by the nondipole contributions to the field, but this bias is supposed to cancel out when enough globally distributed results from several centuries are averaged. In our new models the evolution of the dipole moment during past millennia is determined by spherical harmonic analysis.

[6] The data set and modeling method are described in detail in previous papers. After briefly summarizing this information we explain how we chose the parameters for our preferred models and compare them with the previous model CALS3K.1. Power spectra, the evolution of the dipole moment and magnetic flux distribution at the CMB are discussed.

## 2. Data and Modeling Method

[7] The data set, described in detail by *Korte et al.* [2005], consists of globally distributed archeomagnetic and paleomagnetic data covering the past 7000 years. In contrast to our earlier work [*Korte and Constable*, 2003] the data series are not smoothed prior to modeling and intensity data are also included. There are quite a number of archeomagnetic results from the 19th and 20th century, and we now consider data up to 1950 AD (previously 1800 AD), obtaining an even longer overlap with historical models like GUFM [*Jackson et al.*, 2000]. Directional data come from lake sediments (41 locations) and archeomagnetic artifacts and lava flows (23 regions). Intensity data come from archeomagnetic artifacts and lava flows (17 regions). Archeomagnetic data are not

reduced to representative locations, but are grouped by regions for comparison and visualizing model fit. These regions are not of equal size nor are they distributed evenly over the globe, but rather are determined by the amount of data available. The spatial distribution of archeomagnetic data in particular is clearly biased toward a very high concentration in Europe, while coverage of the southern hemisphere is very sparse. Lake sediments are distributed slightly more evenly, with 3 Argentinian, 3 African, 5 Australian, 1 New Zealand and 1 Antarctic peninsula sediment time series covering the southern hemisphere. Temporal resolution and coverage of the data also varies considerably and for the archeomagnetic data is generally worse for older times. Although the data set contains intensity data, it is still dominated by directional data. In the time span 1000 BC to 1950 AD we have 9464 inclination values, 7596 declination values but only 2316 intensity values. For the whole 7000 years there are 16,085 and 13,080 inclination and declination values, respectively, compared with 3188 intensity values. Spatial and temporal distribution of all the data are displayed in detail by *Korte et al.* [2005], and the effect on global models is discussed further in the following sections.

[8] In an attempt to assign coherent error estimates to the whole data set we introduced minimum errors for each different data type which were assigned whenever the original error estimates were smaller or no estimates given at all. In our modeling approach we cannot take dating errors into account separately from measurement errors. To accommodate them, we increased the uncertainty estimates in categories depending on dating uncertainty. We followed a similar approach in a few cases where locations were not given exactly. The categorized amounts by which to increase the overall uncertainty estimates were determined by studying spatial and temporal field gradients from CALS3K.1 [*Korte and Constable*, 2003] and GUFM [*Jackson et al.*, 2000]. The final error estimates are a minimum of 2.5° in inclination, 3.5° in declination and 1.5 μT in intensity. Average error estimates are 4.2° in inclination, 6.7° in declination and 11 μT in intensity. Details about error estimation are given by *Korte et al.* [2005], and we will discuss some data rejection in the modeling section. Reviewer Richard Holme noticed that we made an error in adding up the different uncertainties: we simply added the values themselves, instead of following the rule that for independent errors the square of the resulting error is the sum of the individual errors squared. Doing this right decreases the final error estimates considerably, influencing the amount of data rejected iteratively and the resolution of models fitting the data within the uncertainty limits. The error estimates for the archeomagnetic and paleomagnetic data are in general not very well-determined. The results we obtained using our "erroneous" error estimates suggested that they are of a reasonable order to give reliable (low-resolution) models when the data are fit within those uncertainties. We therefore leave the correction of the error estimates to a future study to explore in more detail whether higher-resolution models seem feasible from archeomagnetic and paleomagnetic data.

[9] The modeling method is the same as used previously for CALS3K.1. It is based on a spherical harmonic expansion up to degree and order 10 in space and cubic B splines in time. We retain a knot point interval of roughly 60 years by setting the number of knot points to 55 for the interval 1000 BC to 1950 AD and to 130 for the interval 5000 BC to 1950 AD. Regularization is applied in both space and time. As for CALS3K.1 we use the Ohmic heating norm of *Gubbins* [1975] for the spatial regularization and the norm of minimum surface integral of the second time derivative of the radial field $B_r$ for the temporal regularization. The damping factors for space and time are denoted $\lambda$ and $\tau$, respectively. The data are weighted by their error estimates and we calculate rms misfits normalized by the errors and the number of data for our models. More details and the mathematical formulation have already been given by *Korte and Constable* [2003]. For CALS3K.1 we had to use an assumption about the evolution of the axial dipole moment to compensate for the lack of intensity information. This was implemented as additional data input of $g_1^0$-coefficient values controlled by a multiplying factor to allow for separate weighting of this scaling constraint. The inclusion of intensity information allows us to eliminate this constraint. However, we note that it can still be useful in initial stages of the modeling, where we used it with lower weight to compensate for the dominance of the directional data over the intensity data. Additionally, we implemented a multiplicative weighting factor for the intensity data themselves. In contrast to the weight given by the error estimates this

additional factor is ignored when calculating the normalized rms misfits.

## 3. Choice of Model Parameters and Iterative Data Rejection

[10] The solution to an inverse problem as presented here is far from unique. No strictly objective criteria exist to tell us which solution best describes the real field distribution. Deciding which model to present as the one considered to be the best representation of reality is not an easy task. By using a regularization we try to find the simplest model, i.e., the model with minimum structure which fits the data to within a certain accuracy. No structure should be present that is not actually required by the data. If we rigorously believe in our uncertainty estimates we have to find a model that fits the data to within these limits. With the archeomagnetic and paleomagnetic data the uncertainty estimates are, however, not very well determined. They contain not just uncertainties in the techniques of measuring the magnetization, but also contributions caused by dating uncertainties and inaccurate assumptions about the acquisition and retention of the remanent magnetization. We use the error estimates to weight the data relative to each other, but do not always require the models to give a misfit within these error estimates.

[11] When intensity data are included, we have 4 parameters to trade off. Apart from the spatial and temporal damping factors, the factor to weight the under-represented intensity data has to be chosen and we have to decide whether we still want to utilize the axial dipole constraint for additional robustness of the models, and how strongly to weight it. Several criteria can be used to determine the 4 parameters for our preferred models. The choice is complicated by the fact that the influence of the different parameters on the model is not completely independent. Initially, as for CALS3K.1, we demand that model predictions for $B_r$ at the CMB give a predominantly dipolar structure for recent epochs. This is the case in all recent and historical models with better spatial resolution, so it clearly is a valid assumption. We always chose the minimum spatial damping factor for which recent parts of the models fulfill this requirement by visual comparison. Reassuringly, this leads to predominantly dipolar models for most of the total time interval, a behavior that we would expect for a time span which is still short compared with the timescales of large excursions and reversals. Note that we are not able to fit all data within the estimated uncertainties with this requirement. The same was true for CALS3K.1 despite the smoother data series used there.

[12] Choosing the temporal damping factor is more subjective. We studied the evolution of the coefficients with time and chose the factor such that no significant structure is present for periods of less than approximately 100 years, arguing that given the age uncertainties of large fractions of the data we should not expect better temporal resolution. The choice is confirmed by the fact that with smaller temporal damping factors the general evolution of coefficients remains the same except for superposed quite uniform, periodic oscillations for the whole time: these must be considered unrealistic as they are not observed in recent and historical field models of higher resolution.

[13] The remaining two parameters, the weighting factor for intensity data and the factor for the axial dipole constraint both govern the influence of the intensity information on the model. Our aim is to fit all data types equally well within their estimated uncertainties. We use the influence of these two parameters on the total rms misfit and the rms misfit of intensity data alone as a criterion to choose their preferred values. It is obvious that increasing weight on intensity data decreases the rms misfit to intensity. Up to a certain point, however, it also decreases the total rms misfit to all data. Although this is not completely independent of the amount of spatial damping applied, it is obvious enough in the spatial damping range of dipole dominated models. We thus can choose the weighting factor for intensity to minimize the total rms misfit, which is accomplished with a weight of 2.

[14] We expected the axial dipole constraint would no longer be necessary. Surprisingly, when using all data we could again decrease the misfit to the intensity data if we retain our crude axial dipole assumptions from CALS3K.1 with low weight. Consequently, we set up a new axial dipole constraint for both the 3000 and the 7000 year intervals, following more closely the results for the virtual axial dipole moment evolution obtained by *Yang et al.* [2000]. The decrease in intensity misfit sometimes is obtained at the cost of a slight increase of directional misfit, in particular for declinations. With a suitable weighting factor, the improvement to the intensity fit is strong compared with the loss of overall fit and sometimes it even increases overall fit. We decided to retain the axial dipole constraint in all our initial models with a

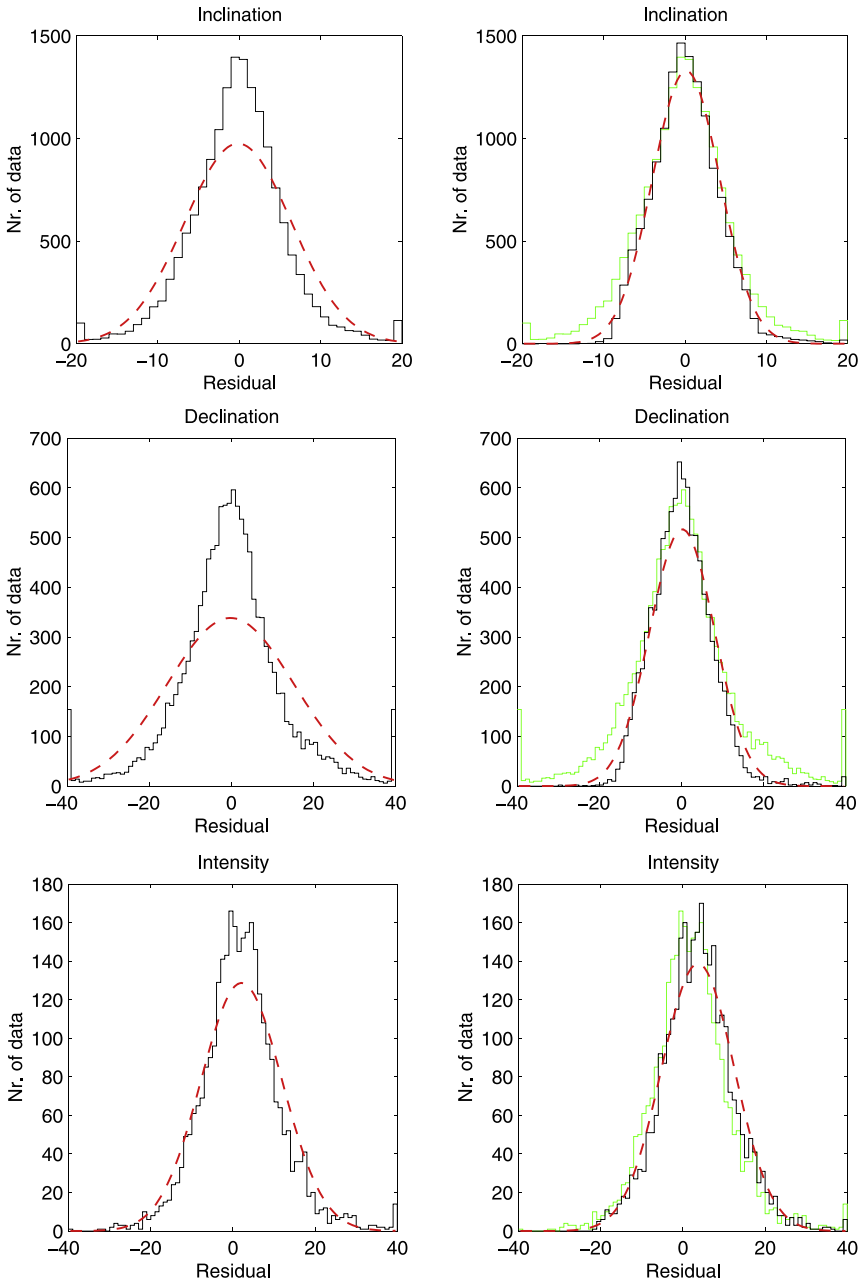


**Figure 1.** Distribution of residuals in inclination, declination, and intensity from the 7000 year data. Inclination and declination are in degrees; intensity is in μT. (left) Histograms of residuals to a model after 3 iterations for all data. The dashed red curves are normal distributions with the same mean and standard deviation. (right) Histograms (black) of residuals of declination after data rejection to final preferred model (CALS7K.2) and normal distribution (dashed red curve) with the same mean and standard deviation. The green histograms are the ones from the left for direct comparison.

weighting factor of 0.001. The resulting fit is not quite as close to the axial dipole constraint as it was for CALS3K.1. With this weighting factor, however, differences between coefficients other than the axial dipole obtained with the old or new constraint are negligible.

[15] As mentioned above it is not possible to fit all data within the estimated uncertainties with this approach. Looking at the distribution of the residuals to a "good" model after several iterations it is obvious that they are far from normally distributed. Figure 1 (left column)

**Table 1.** Number of Data and Misfit, CALS3K.2[a]

| Data Type | $N_i$ | $\text{rms}_i$ | $R$, % | $N_r$ | $\text{rms}_r$ | $\text{rms}_f$ |
|---|---|---|---|---|---|---|
| All data | 19376 | 2.15 | 13.9 | 16677 | 1.49 | 1.00 |
| Inclination | 9464 | 1.90 | 13.7 | 8167 | 1.44 | 1.01 |
| Declination | 7596 | 2.54 | 17.4 | 6272 | 1.53 | 1.02 |
| Intensity | 2316 | 1.62 | 3.4 | 2238 | 1.57 | 0.90 |

[a] $N$ is the number of data, and rms is the root mean square misfit to a constant axial dipole of 30 μT before and after data rejection, denoted by subscripts $i$ and $r$, respectively. $R$, % is the number of rejected data in percent of the initial data, and $\text{rms}_f$ is the misfit to the final model.

shows histograms of the residuals from the development of CALS7K.2. Comparison with the normal distribution curve with same mean and standard deviation as the residuals reveals that a large number of data are fit better than expected, suggesting the presence of several outliers in the data set. This agrees with our expectation from the assessment of data quality. Consequently we decided in a second step to reject data that cannot be fit to within two times the average uncertainty estimate for the individual components with an initial model. The initial model is obtained by three iterations using all data and choosing the parameters in the way described above. It turns out that we can keep the parameters fixed for these iterations to give the desired results. The choice of three iterations again was made empirically: up to that iteration step the rms misfit decreased significantly in all cases, whereas there is only slight improvement in misfit and correspondingly minor changes in the data rejected for subsequent iteration steps. After data rejection we start iterations again from the constant axial dipole starting model. Two facts are noteworthy: First, the level of data rejection is such that afterward we can readily fit the remaining data to better than the estimated tolerance with predominantly dipolar models and reasonably smooth coefficients. The distribution of residuals is much closer to normal now as shown in the right column of Figure 1. Second, the use of the axial dipole constraint no longer has much influence on the fit, in particular it does not improve the fit to the intensity data. Consequently, we removed this constraint at this point and used only the intensity data information to govern field strength and dipole evolution of the model. The approach now is to sweep through a range of spatial and temporal damping factors to find the model with a normalized rms misfit of 1 for each iteration step. Convergence is fast, after three to four iteration steps there was no further significant change to the models with this method.

## 4. Results

[16] Using the procedure described above we obtained two new preferred models: an improved model for the past 3000 years named CALS3K.2 and a first model for the past 7000 years named CALS7K.2 (see Introduction about CALS7K.1), which will be presented in this section. The results will show that CALS3K.2 as an improvement over the previous CALS3K.1 is already obsolete by the development of CALS7K.2. We present both models, however, not only to demonstrate this fact but also because we did use some additional a priori data rejection in CALS3K.2 as described below.

### 4.1. CALS3K.2

[17] Considering only the past 3000 years, the declination series from Lake Superior (SUP) and Lake Huron (HUR) look distinctly different both from each other and from the more consistent series from Lakes LeBoeuf (LEB) and St. Croix (LSC) [see *Korte et al.*, 2005]. Those four North American lakes all lie within distances of a few hundred kilometers from each other. The difference is much larger than we can reasonably expect for an area of that size and much more significant than differences in any other region covered by our data set. We therefore decided to reject the two data series of SUP and HUR a priori in this case. The initial normalized rms misfit to a constant dipole with $g_1^0 = 30$ μT then is 2.17. As preferred final model, named CALS3K.2, we chose the third iteration model after data rejection. An overview of number of data and misfit for the individual components is given in Table 1.

[18] The differences in the percentage of data rejected among the components correlates with the degree of deviation of residuals from a normal distribution. It tends to reflect the number of outliers or data quality in the individual components, although there are some deviations from this pattern due to the inhomogeneous spatial and temporal distribution of data. The model may be able to fit erroneous data quite well if there are no good data in the temporal and spatial vicinity. The normalized fit to the different field components is not quite equal. Apart from the inhomogeneity, which also can have an influence here, this reflects our ability to estimate consistent uncertainties. The slightly lower $\text{rms}_f$ suggests that the estimated

**Table 2.** Parameters and Norms of CALS3K.2[a]

| Iteration | rms | $\lambda$, $nT^{-2}$ | Spatial Norm, $nT^2$ | $\tau$, $nT^{-2}yr^4$ | Temporal Norm, $nT^2yr^{-4}$ | Intensity Factor |
|---|---|---|---|---|---|---|
| 1*b.r.* | 1.83 | $10^{-7}$ | $35 \times 10^9$ | $5 \times 10^{-2}$ | $17 \times 10^3$. | 2 |
| 2*b.r.* | 1.81 | $10^{-7}$ | $36 \times 10^9$ | $5 \times 10^{-2}$ | $40 \times 10^3$ | 2 |
| 3*b.r.* | 1.80 | $10^{-7}$ | $37 \times 10^9$ | $5 \times 10^{-2}$ | $62 \times 10^3$ | 2 |
| 1*a.r.* | 1.00 | $5 \times 10^{-8}$ | $36 \times 10^9$ | $1 \times 10^{-2}$ | $54 \times 10^3$ | 2 |
| 2*a.r.* | 1.00 | $3 \times 10^{-7}$ | $22 \times 10^9$ | $5 \times 10^{-1}$ | $54 \times 10^3$ | 2 |
| 3*a.r.* | 1.00 | $3 \times 10^{-7}$ | $22 \times 10^9$ | $5 \times 10^{-1}$ | $55 \times 10^3$ | 2 |

[a] Annotations *b.r.* and *a.r.* mean before and after data rejection, respectively.

intensity uncertainties are too large compared with those of inclination and declination.

[19] Table 2 lists the values of $\lambda$ and $\tau$ used at each iteration step before and after data rejection. The spatial norm of CALS3K.2 is about the same as for CALS3K.1. Note that there is a typographical error in Table 2 of *Korte and Constable* [2003]: the spatial norm for CALS3K.1 with an rms misfit of 1.30 should read $28 \times 10^9$ $nT^2$ instead of $2 \times 10^9$ $nT^2$. Surprisingly, the temporal norm is less than half as big as for CALS3K.1.

[20] Figure 2 shows a comparison of dipole coefficients and dipole moment for CALS3K.1 and CALS3K.2. A striking fact is that neither the axial dipole coefficient nor the dipole moment agree. The new initial axial dipole constraint displayed in the figure, as well as $g_1^0$ of CALS3K.1, are based on virtual (axial) dipole moment (VDM and VADM) studies, so we focus on that comparison

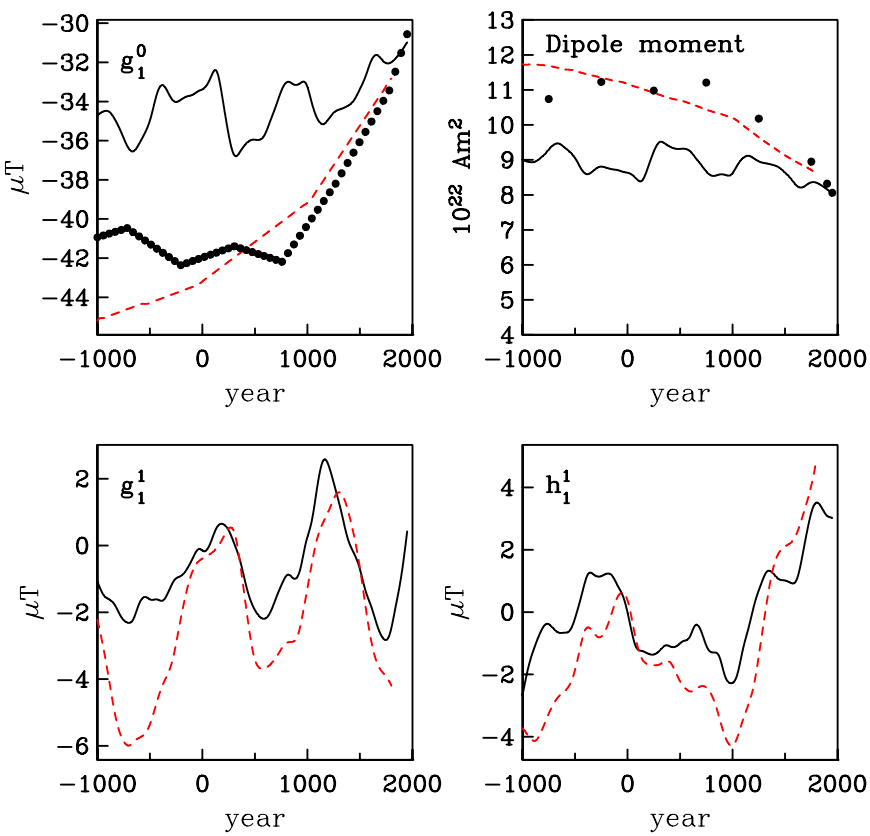


**Figure 2.** Axial dipole coefficient $g_1^0$, dipole moment, and dipole coefficients $g_1^1$ and $h_1^1$. Solid black line is from CALS3K.2; dashed red line is from CALS3K.1. The dots are the VADM results from *Yang et al.* [2000] (top right panel) and our new, linearly interpolated axial dipole constraint based on them (top left panel). The constraint was not used in the final CALS3K.2 model.

**Table 3.** Number of Data and Misfit, CALS7K.2[a]

| Data Type | $N_i$ | $rms_i$ | $R$, % | $N_r$ | $rms_r$ | $rms_f$ |
|---|---|---|---|---|---|---|
| All data | 32353 | 2.34 | 16.3 | 27067 | 1.51 | 1.00 |
| Inclination | 16085 | 1.89 | 14.3 | 13776 | 1.41 | 0.97 |
| Declination | 13080 | 2.93 | 22.0 | 10199 | 1.65 | 1.06 |
| Intensity | 3188 | 1.54 | 3.0 | 3092 | 1.48 | 0.92 |

[a] $N$ is the number of data, and rms is the root mean square misfit to a constant axial dipole of 30 μT before and after data rejection, denoted by subscripts $i$ and $r$, respectively. $R$, % is the number of rejected data in percent of the initial data, and $rms_f$ is the misfit to the final model.

first. The differences between the *Yang et al.* [2000] results and the dipole moment of CALS3K.1 are due to differences between the *Yang et al.* [2000] VADM results and the *McElhinny and Senanayake* [1982] results on which the CALS3K.1 axial dipole is based. The apparently too small spherical harmonic dipole moment of CALS3K.2 is also found in the 7000 year model CALS7K.2 and will be discussed later. Apart from the axial dipole coefficient the coefficients show the same general trends for CALS3K.1 and CALS3K.2 and, except for the earliest epochs, about the same amplitude. Model coefficients for CALS3K.2 together with additional material (evaluation code, movies, snapshot figures) are stored in the EarthRef Digital Archive (ERDA); see Appendix A for details.

### 4.2. CALS7K.2

[21] In this 7000 year case we retained all data for the model before the iterative data rejection as we did not notice such striking discrepancies over the whole time span as described for the 3000 year data set. For earlier epochs the two lakes rejected for CALS3K.2 do not show such a strong disagreement. Tables 3 and 4 list number of data, rms misfit, and parameters used for CALS7K.2, chosen as the fourth iteration model after data rejection. The percentages of rejected data are similar to those of CALS3K.2. The higher percentage of rejected declination data is partly due to the fact that many data from sites SUP and HUR were rejected at this stage, while they had been rejected a priori for CALS3K.2.

[22] The variation of coefficients and the model predictions agree well with CALS3K.2 for the overlapping time span of 1000 BC to 1950 AD, so we will focus on CALS7K.2 in the following discussion of properties. Model coefficients for CALS7K.2, evaluation code, animations of model predictions and more snapshot figures than presented in the next section can be found in the EarthRef Digital Archive (ERDA); see Appendix A for details.

## 5. Discussion

### 5.1. Fit to the Data

[23] The fit of the model to the individual data series is about equally good for all the archeomagnetic directional and intensity data. Figure 3 shows some examples which can be considered representative for the scatter of archeomagnetic data and the quality of fit and resolution of the model. With the lake sediment data the fit is significantly different. This difference between archeomagnetic and lake sediment results is partly caused by our way of looking at the data: for archeomagnetic data results from regions are grouped to one time series regardless of their origin. If the individual lake sediment series were grouped in the same way scatter and average fit for the regions would mostly be comparable.

[24] With the individual lakes, some data series are fit very closely down to short timescales, like the 2 examples of Lake Biwa (BIW) and Laguna el Trebol (TRE) shown in Figure 4. Lake Biwa, Japan, lies in a sparsely covered region. The nearby

**Table 4.** Parameters and Norms of CALS7K.2[a]

| Iteration | rms | λ, $nT^{-2}$ | Spatial Norm, $nT^2$ | τ, $nT^{-2}yr^4$ | Temporal Norm, $nT^2yr^{-4}$ | Intensity Factor |
|---|---|---|---|---|---|---|
| 1*b.r.* | 1.97 | $10^{-7}$ | $82 \times 10^9$ | $10^{-1}$ | $29 \times 10^3$ | 2 |
| 2*b.r.* | 1.94 | $10^{-7}$ | $82 \times 10^9$ | $10^{-1}$ | $41 \times 10^3$ | 2 |
| 3*b.r.* | 1.93 | $10^{-7}$ | $87 \times 10^9$ | $10^{-1}$ | $63 \times 10^3$ | 2 |
| 1*a.r.* | 1.04 | $5 \times 10^{-8}$ | $66 \times 10^9$ | $5 \times 10^{-1}$ | $35 \times 10^2$ | 2 |
| 2*a.r.* | 1.01 | $2 \times 10^{-7}$ | $42 \times 10^9$ | $5 \times 10^{-2}$ | $23 \times 10^3$ | 2 |
| 3*a.r.* | 1.00 | $3 \times 10^{-7}$ | $40 \times 10^9$ | $3 \times 10^{-2}$ | $51 \times 10^3$ | 2 |
| 4*a.r.* | 1.00 | $3 \times 10^{-7}$ | $40 \times 10^9$ | $5 \times 10^{-1}$ | $53 \times 10^3$ | 2 |

[a] Annotations *b.r.* and *a.r.* mean before and after data rejection, respectively.

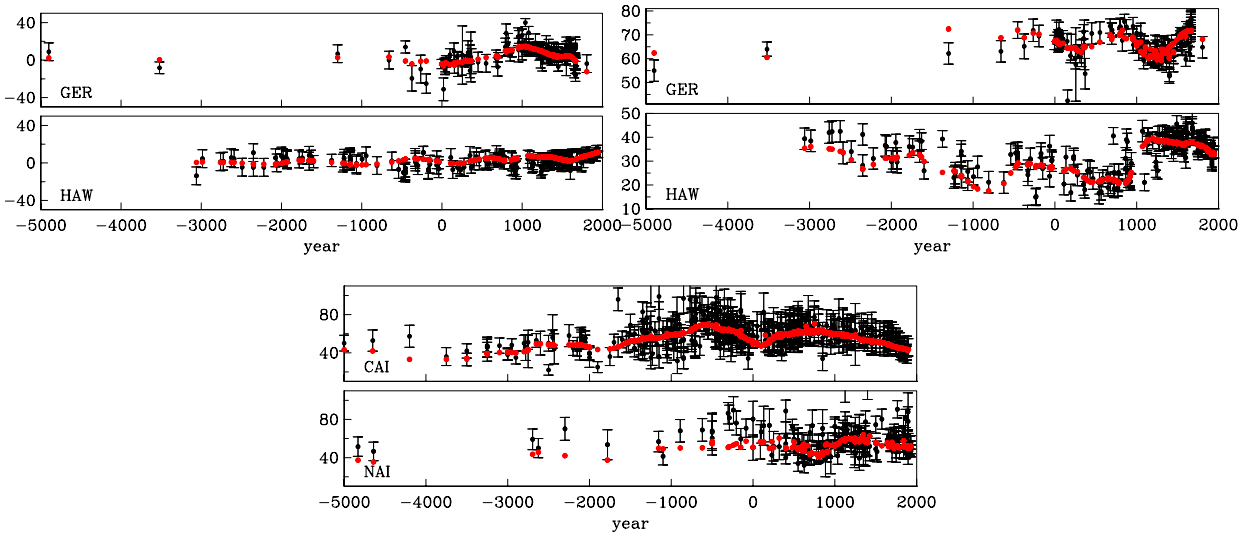


**Figure 3.** Fit to the data: some examples of archeomagnetic (top) directional and (bottom) intensity data (black, with error bars) and model predictions (red) of CALS7K.2. Directional data are (left) declination and (right) inclination in degrees; intensity is in μT.

Japanese archeomagnetic data barely cover the most recent 2000 years, therefore the good fit might be expected. Note, however, that due to the global nature of the basis functions this is not necessarily the case. The close fit to the Laguna el Trebol data in Argentina is particularly satisfactory. Three lakes are closely adjacent in this otherwise uncovered area and the fit to these independent records is equally good. This strongly supports the reliability of the model in this part of the sparsely covered southern hemisphere.

[25] In other cases, like the example of Lake Baikal (BAI) in Figure 4, not even the general trend has

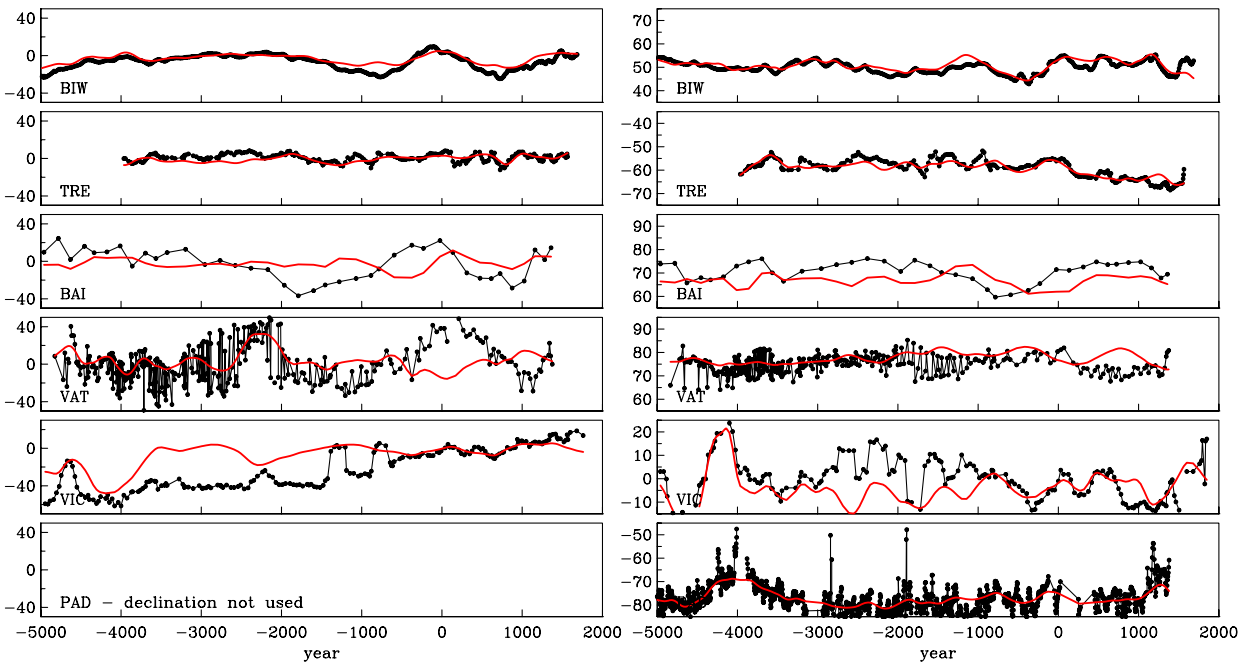


**Figure 4.** Fit to the data: some examples of lake sediment records (black) and CALS7K.2 predictions (red). (left) Declination and (right) inclination are in degrees.

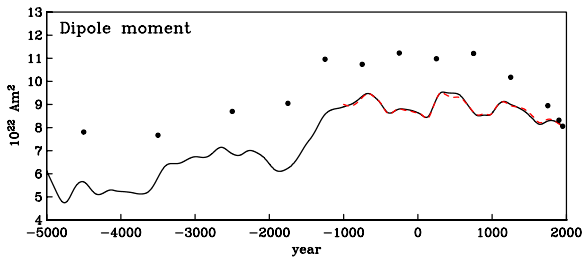


**Figure 5.** Dipole moment of CALS7K.2 (continuous curve) and time-averaged VADM results from *Yang et al.* [2000] (dots). The red dashed curve of the dipole moment of CALS3K.2 is barely visible because it agrees well with that of CALS7K.2. The dots at years 1900 and 1950 are the dipole moments given by the IGRF model coefficients for those epochs.

been fit for some time intervals. This is in fact quite an interesting example: In the interval between 2000 BC and 100 AD the model prediction is still close to that of CALS3K.1, for which an adjusted age scale for Lake Baikal data had been used [*Constable et al.*, 2000]. CALS7K.2 now seems to confirm the validity of this adjustment, as it is not possible to fit the data on the original timescale closely under the constraints imposed by the surrounding data.

[26] The lower two examples in Figure 4 are from Lake Victoria, Uganda (VIC) and Palmer Deep, Antarctic Peninsula (PAD). Both show strong inclination maxima around 4200 BC and 4000 BC, respectively, which would qualify as excursions. There are no other data in the near vicinity of either of these locations, so models tend to fit those data well. For Palmer Deep, however, this feature is accompanied by very large uncertainty estimates from principal component analysis, and after weighting the data by those uncertainties the model only fits the structure to the degree shown here. In CALS7K.1 we had missed those large uncertainty estimates and fit those data more closely than we now believe to be justified. For Lake Victoria, however, we have no further information on the reliability of these data. As it was our policy not to reject or downweight data for purely subjective reasons we did not do so in this case. We want to point out, however, that this strong inclination anomaly in the African region around 4200 BC might not prove robust in future models if more data from that region became available. Note also that the same might be the case for other, less pronounced features at times and areas not well-covered by data, particularly in the Southern hemisphere.

## 5.2. Dipole Moment

[27] For CALS3K.2 we already noted that the dipole moment is significantly lower than the VADM results of *Yang et al.* [2000]. The results from CALS7K.2 confirm this but show that the long-term trends clearly are the same (Figure 5). There are two possible explanations, which probably both contribute to the observed offset.

[28] First, our data are dominated by directional measurements while the field strength, i.e., the scaling, is governed by the intensity data. In theory the scaling should be independent of the directions [*Hulot et al.*, 1997]. That is strictly true, however, only for an infinitely dense global coverage of accurate data and a field with two and only two poles. In practice we find that the fit to intensity can be improved to a certain degree at the cost of fit to directions and vice versa, reflecting the uneven data distribution and their uncertainties. In finding a model with the best overall fit to the data the underrepresented intensity data might be under-fit and thus the model might lack strength and consequently show a lower dipole moment. We carried out several tests to assess this concern. Checking the fit to all archeointensity data visually did not reveal any serious, systematic underfitting of the data (see Figure 3). The mean of the intensity residuals (as displayed in Figure 1), has a slight bias of 3.6 $\mu$T or about 7% of the predicted intensity values, while declination and inclination residuals do not have any significant bias. This bias, however, can account for less than half of the observed difference in dipole moment magnitude only, and it is not possible to obtain a model with zero intensity residual bias and equally good fit to all the data as given by CALS7K.2.

[29] Second, VDMs and VADMs do not take into account the nondipole contributions to the field. In averaged results these contributions will have cancelled out to a certain degree. It seems unlikely, however, that they completely cancel out over time spans of a few centuries with such an uneven global data distribution. Consequently, we might expect that VDMs and VADMs will be too high compared with SHA dipole moments. The fact that our model's dipole moment agrees very well with the IGRF dipole moment (dots for 1900 and 1950 in Figure 5) further supports that

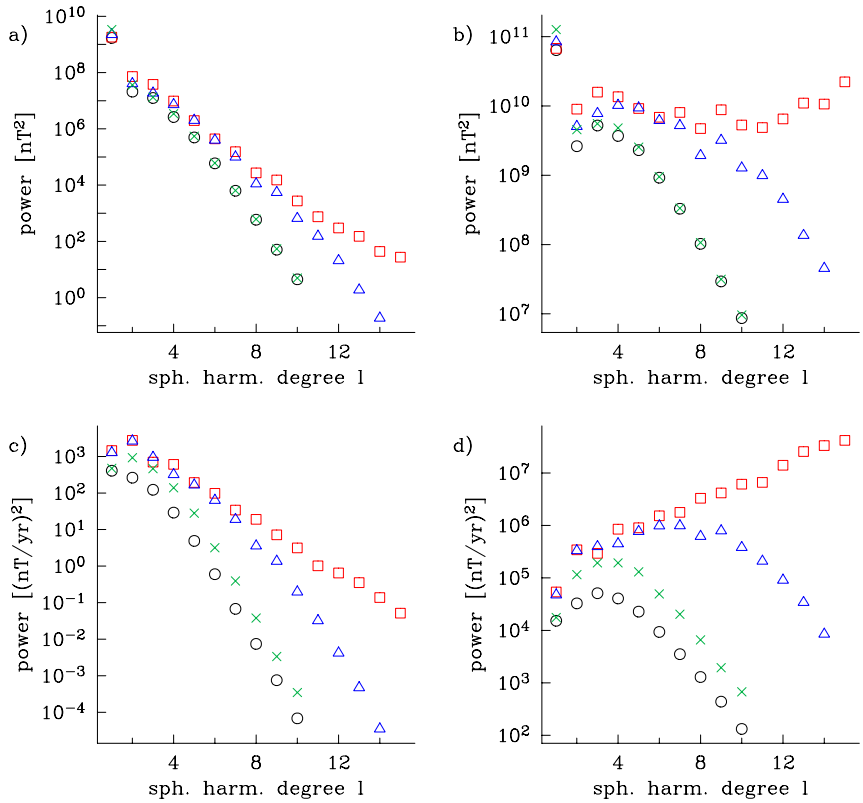


**Figure 6.** Comparison of power spectra of several global spherical harmonic models: CALS7K.2 (circles), CALS3K.1 (green crosses), GUFM [*Jackson et al.*, 2000] (blue triangles), and POMME1.4 [*Maus et al.*, 2005] (red squares). (a) Field spectrum at the Earth's surface, (b) field spectrum at the CMB, (c) secular variation spectrum at the Earth surface, and (d) secular variation spectrum at the CMB.

a large part of the offset might be attributable to this effect, which we study further in a subsequent paper [*Korte and Constable*, 2005].

## 5.3. Spatial Power Spectra

[30] To address quality and reliability of the new models, we compare the spatial power spectra of CALS7K.2 to several other global spherical harmonic models in Figure 6. For the temporally continuous models CALS7K.2, CALS3K.1 and GUFM [*Jackson et al.*, 2000] the spectra are averaged over the whole time interval of the models. POMME1.4 [*Maus et al.*, 2005] is a high-resolution individual epoch model centered on 2002.0 from CHAMP satellite data. CALS3K.2 (not shown) gives a very similar spectrum to CALS7K.2 with slightly more power in secular variation, thus agreeing more closely with CALS3K.1.

[31] The models from paleomagnetic and archeomagnetic data generally show less power in all spherical harmonic degrees for the field and its secular variation than the higher-resolution models from directly measured, recent field data. The only exception is the field's dipole contribution, where there is close agreement among all models. Only CALS3K.1 shows too much power in degree 1, which is explained by the axial dipole constraint used there. The lack of power in all the other degrees must be attributed to lack of resolution due to the lower confidence in the archeomagnetic and paleomagnetic data. From the steep drop-off in the spectra, particularly evident at the CMB, it becomes clear that only the coefficients up to degree four or five can be resolved reliably in accordance with what we expect from data quality and distribution. For the field spectra the relative power in degrees 2 to 5 is similar in the millennial scale models to that in the recent models, with less power in degree 2 than 3 at the CMB.

[32] In secular variation there are larger differences, not only from the recent models but also between the millennial scale models. Taking that as an indication that secular variation of the model is less reliable, however, might be premature. If we study the

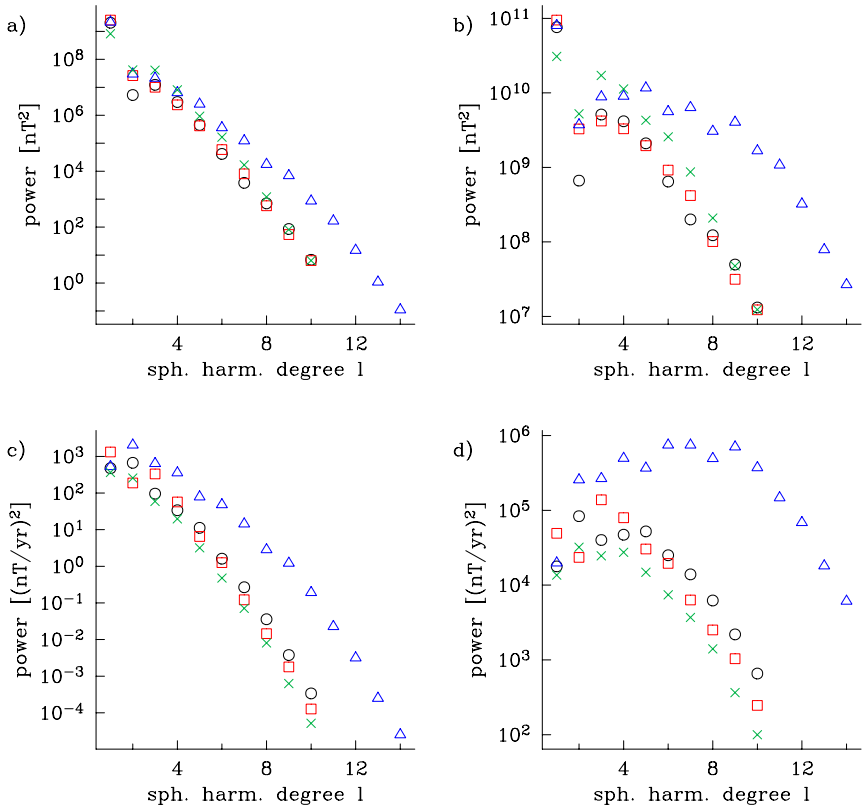


**Figure 7.** Examples of several power spectra of different 100-year averages from CALS7K.2: 1800–1900 AD (circles), 200–300 AD (red squares), 4100–4000 BC (green crosses), and, for comparison, average of GUFM [*Jackson et al.*, 2000] (blue triangles) 1800–1900 AD. (a) Field spectrum at the Earth's surface, (b) field spectrum at the CMB, (c) secular variation spectrum at the Earth surface, and (d) secular variation spectrum at the CMB.

development of the spectra in time there are periods with significant changes. For secular variation, averaged spectra of the recent centuries from CALS7K.2 agree better with those from the recent models than earlier ones. A few examples are given in Figure 7 compared with GUFM.

[33] We propose that there really are significant changes in the spectral distribution of secular variation on the long timescales. This and the change of spectral distribution of the field itself are depicted in Figure 8, where dipole power and power of the sum of all the higher-degree harmonics are compared through time. Figure 8a shows that the dipole power is strongly dominant at the Earth's surface for the whole time. At the CMB (Figure 8b), however, the cumulative power of the higher-degree contributions reached and exceeded that of the dipole in times of weak dipole moment. Of course, to a certain degree the power at the CMB only reflects the limited resolution of our model. For higher-resolution models like GUFM the cumulative power of all higher degrees at the CMB always exceeds that of the dipole moment. However, the cumulative power of only the first few nondipole degrees does not, and that is all we can resolve with the millennial scale models. What our model suggests is that power in spherical harmonic degrees 2 to about 4 in particular has been significantly higher at times in the past than as it is today and is strongly variable.

[34] Secular variation power (Figures 8c and 8d) is very variable in both the dipole and the higher-degree contributions. While higher-degree secular variation contains significantly more power at the CMB, the stronger attenuation of the short-wavelength contributions toward the Earth's surface leads to comparable power in cumulative nondipole and dipole contributions there.

## 5.4. Differences Between CALS7K.2 and Earlier Model CALS3K.1

[35] In the field predictions, CALS7K.2 and CALS3K.2 agree well for the overlapping time span. However, there are some significant differences from CALS3K.1. We first checked the influ-

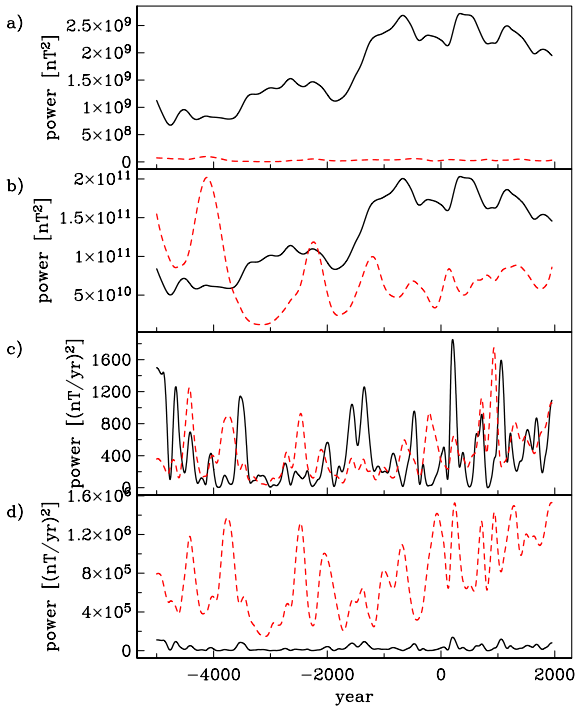


**Figure 8.** Spectral power of CALS7K.2 through time: black line is the dipole power, dashed red line is the sum of higher-degree power (a) at the Earth's surface, (b) at the CMB, and for secular variation at (c) the surface and (d) the CMB.

ence of the intensity data on the model by producing a model using just the new directional data for the same time span and the same axial dipole constraint as used for CALS3K.1. The damping factors were chosen to give comparable spatial and temporal norm values to CALS3K.1. Differences in predicted global field distribution between this model and the new CALS3K.2 are small, confirming that even with these data the intensity mainly serves as a scaling factor and does not give any significant information about field structure over that obtained from directional values. Another reason, however, might be the large average error estimates for the intensity data, which could obscure more detailed structure that might in principle be resolvable.

[36] Some snapshots in Figure 9 demonstrate the most significant similarities and differences between the new models represented by CALS7K.2 and CALS3K.1. Model prediction snapshots for all 100 year intervals and movies are available from the EarthRef Digital Archive (ERDA); see Appendix A. The components are the same as in previous papers by *Korte and Constable* [2003] and *Constable et al.* [2000], i.e., radial component ($B_r$) and radial component after subtraction of the axial dipole contribution ($B_{rNAD}$), both at the CMB, inclination anomaly, i.e., inclination after subtraction of the axial dipole contribution, and declination at the Earth's surface. For the most recent centuries the major flux lobes in $B_r$ and $B_{rNAD}$ at the CMB appear similar with slight differences in regions of sparse data coverage like the southern hemisphere (Figure 9a). Declination and inclination anomaly also show very similar distribution at the Earth's surface in both models.

[37] Going back in time, differences become more significant for times when CALS3K.1 no longer shows the two dominating northern hemisphere flux lobes, between 1300 AD and 1000 AD (Figure 9b) and 100 AD to 300 BC (Figure 9d). The new models suggest that those flux lobes are more stationary than CALS3K.1 implied and also that there is less secular variation and concentration of flux in the Pacific area. This result is interesting as it extends the time span of stationary flux lobes observed in historical models much further back. For the epochs in between there is better agreement between old and new models. The two flux lobes appear in the old model, too, while the new models still show more flux and more change in the Pacific region than historical and recent models (Figure 9c). While $B_r$ and $B_{rNAD}$ show more similarity, inclination anomaly still shows a significant difference: a second strong, negative center over the Indian Ocean region existing between 700 AD and 300 AD. For earlier epochs the feature is further north and agrees well with a similar feature seen in CALS3K.1. For the epochs between 300 BC and 1000 BC there are persistent significant differences between the models (Figure 9e). Both show a strong Asian flux lobe, but no clear second negative northern hemisphere flux lobe. Positive flux in the Pacific region, however, is much weaker in the new model and again a region of negative inclination anomaly in the Indian Ocean region is seen in the new models. CALS3K.1 does not show this feature but on the contrary displays strong positive inclination anomalies which are completely absent in CALS7K.2 and CALS3K.2. The increase in differences in the earlier epochs most likely is due to the large increase in number of data, as well as differences in dating of parts of the two data sets, described by *Korte et al.* [2005].

## 5.5. Field Structure Prior to 1000 BC

[38] In the earlier 4 millennia there are more significant changes visible in the radial component

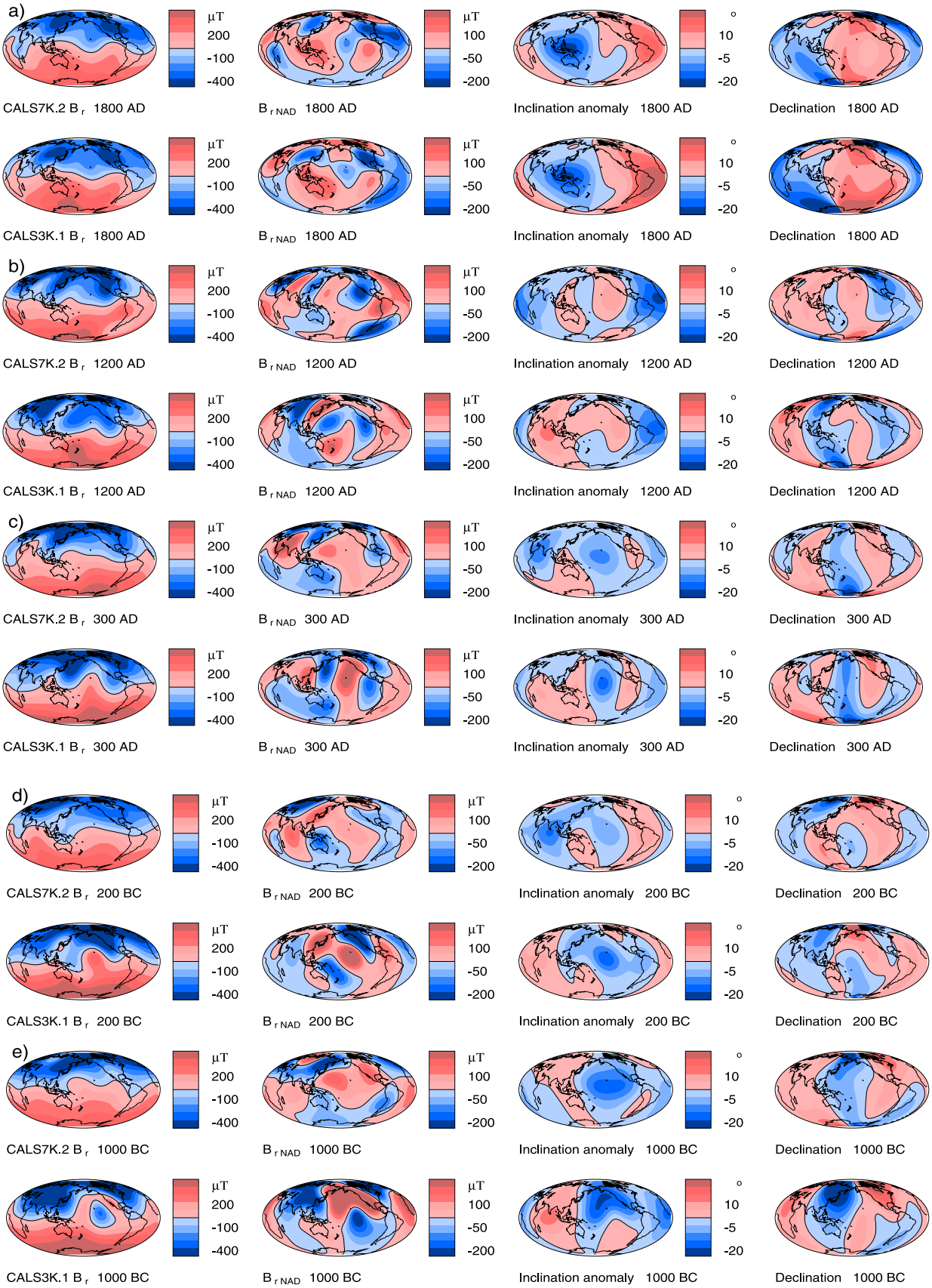
a)
μT 200 -100 -400
CALS7K.2 B r 1800 AD
μT 100 -50 -200
B r NAD 1800 AD
° 10 -5 -20
Inclination anomaly 1800 AD
Declination 1800 AD
CALS3K.1 B r 1800 AD
B r NAD 1800 AD
Inclination anomaly 1800 AD
Declination 1800 AD
b)
CALS7K.2 B r 1200 AD
B r NAD 1200 AD
Inclination anomaly 1200 AD
Declination 1200 AD
CALS3K.1 B r 1200 AD
B r NAD 1200 AD
Inclination anomaly 1200 AD
Declination 1200 AD
c)
CALS7K.2 B r 300 AD
B r NAD 300 AD
Inclination anomaly 300 AD
Declination 300 AD
CALS3K.1 B r 300 AD
B r NAD 300 AD
Inclination anomaly 300 AD
Declination 300 AD
d)
CALS7K.2 B r 200 BC
B r NAD 200 BC
Inclination anomaly 200 BC
Declination 200 BC
CALS3K.1 B r 200 BC
B r NAD 200 BC
Inclination anomaly 200 BC
Declination 200 BC
e)
CALS7K.2 B r 1000 BC
B r NAD 1000 BC
Inclination anomaly 1000 BC
Declination 1000 BC
CALS3K.1 B r 1000 BC
B r NAD 1000 BC
Inclination anomaly 1000 BC
Declination 1000 BC

**Figure 9**

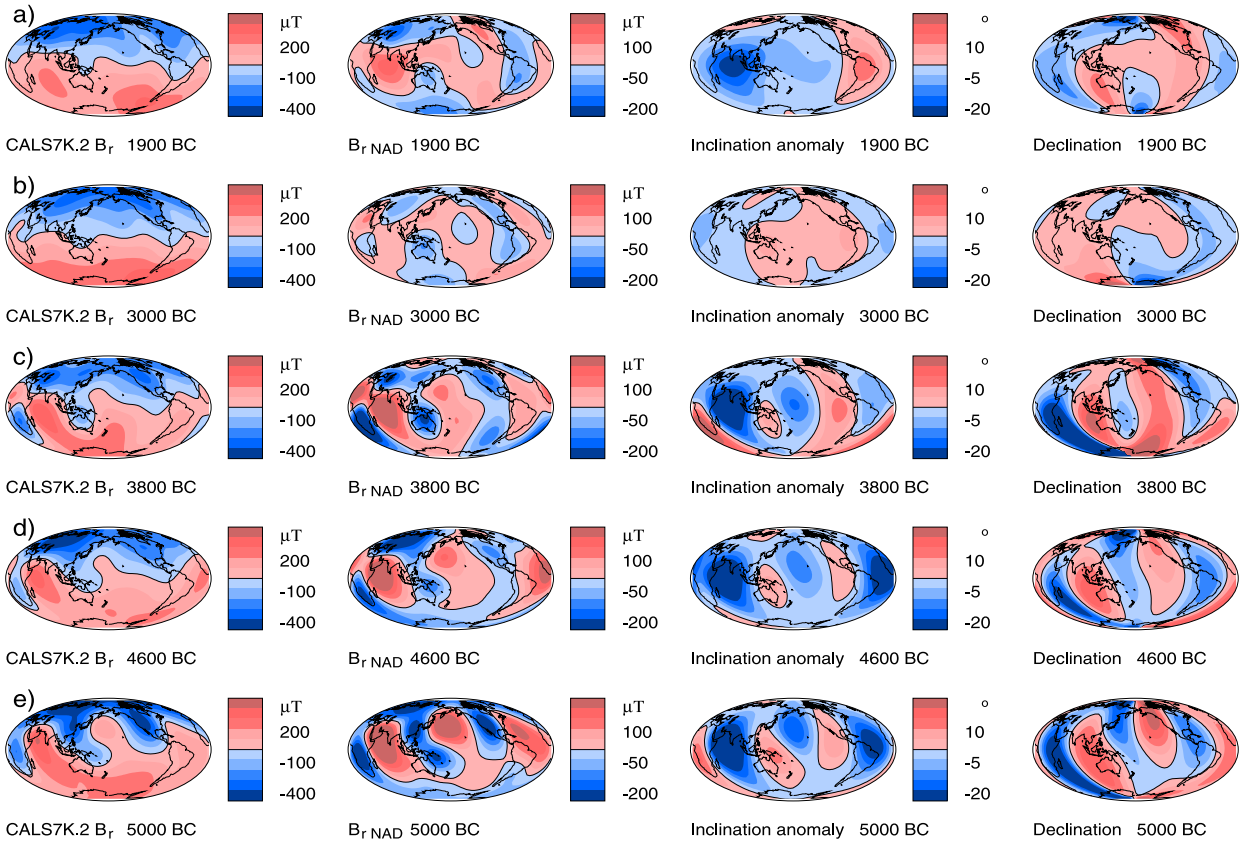


**Figure 10.** (a–e) Some snapshots of field predictions from CALS7K.2 between 1000 and 5000 BC (not evenly spaced in time). Columns from left to right show radial component $B_r$ and nonaxial dipole contribution $B_{rNAD}$, both at the CMB, and inclination anomaly and declination, both at the Earth's surface and with the same color scale.

at the CMB. Starting around 1700 BC the clear dipole structure gives way to a more complex structure with two clearly distinct flux maxima in the southern hemisphere, i.e., stronger influence of higher-degree contributions. An example is shown in Figure 10a for epoch 1900 BC. Is it reasonable to believe this structure given the low resolution of the model? Two arguments support it: First, the model appears more dipole dominated again in earlier epochs, between 2800 BC and 3400 BC, as shown in the example in Figure 10b. The spatial and temporal regularization employed in the modeling technique permits only as much structure as required by the data, it would keep the simple dipolar structure otherwise. The structure is necessary in order to fit the data to the desired degree. However, this does not exclude the possibility that inconsistent dating among data from different regions might lead to spurious structure.

[39] A comparison with the dipole moment strength shows that more complicated $B_r$ structure seems correlated with times when the dipole moment is weak. However, the correlation between field structure visually appearing less dipolar and dipole strength is not perfect; that is, there seems to be no critical value for the dipole moment below which the CMB field is dominated by a higher-degree structure. Let us study the development of field structure and the comparison of dipole power and cumulative nondipole power as displayed in Figure 8 through time. Keep in mind for this whole discussion that the cumulative nondipole power of the millennial scale models is strongly biased low compared to modern high spatial resolution models. In terms of field evolution we have to move forward through time, so we start with some complicated structure where cumulative nondipole power at the CMB is higher than dipole power

**Figure 9.** (a–e) Comparison of CALS7K.2 and CALS3K.1 field predictions for some example time epoch snapshots. Columns from left to right show radial component $B_r$ and nonaxial dipole contribution $B_{rNAD}$, both at the CMB, and inclination anomaly and declination, both at the Earth's surface and with the same color scale.

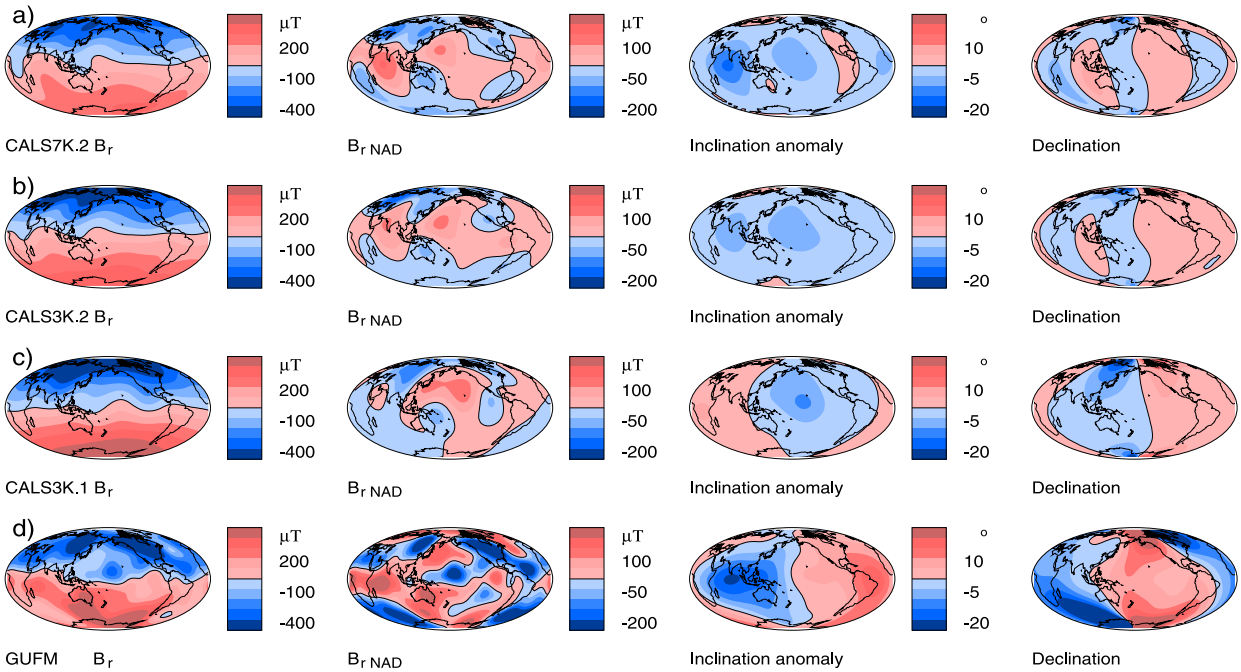


**Figure 11.** Averages over the complete time intervals of continuous global models (a) CALS7K.2, (b) CALS3K.2, (c) CALS3K.1, and (d) GUFM [*Jackson et al.*, 2000]. Columns as for Figure 10.

(Figures 10e, 10d, and 10c). The fact that the field structure at the CMB becomes more dipole dominated about 3500 BC (Figure 10b) is due more to a rapid decrease of nondipole power rather than the increase of dipole power. The dominance of higher-degree structure lasting for a few centuries before 2000 BC (Figure 10a) occurs while the dipole power is comparable to that during the preceding millennium. The dipole power shows a short local minimum, during which the nondipole power also becomes very low. The following strong increase (about 1500 BC to 800 BC of dipole power is accompanied for a while by an increase of nondipole power, but then the latter never exceeds the dipole power at the CMB again.

[40] The structure of inclination anomaly shows some clear correlation with change in dipole dominance. Very strong negative inclination anomalies are observed during the first centuries over the Indian Ocean, the Atlantic and, somewhat more variably, also over the Pacific region. Only around the time when the dipolar structure becomes dominant does the relation between positive and negative inclination anomaly become more balanced. In the time span between 2800 BC to 1800 BC, when nondipole power is strong compared to dipole power once more, there is again an area of strong inclination anomaly over the Indian ocean.

[41] In summary we can say that while dominance of nondipole structure at the CMB is to some degree correlated to a weak dipole moment, the variability of the nondipole power itself is more critical than a distinct level of dipole power. Note also that at the Earth's surface the field structure is dominated by the dipole all the time, as we have already shown in Figure 8a.

## 5.6. Temporal Averages

[42] A comparison of time-averaged models shows that they are quite sensitive to both the time interval and data basis. Figure 11 shows the averages of CALS7K.2, CALS3K.2, CALS3K.1 and GUFM [*Jackson et al.*, 2000] over their respective time spans from 7000 to 400 years. Here the relative lack of structure in $B_{rNAD}$ in the CALS models is not simply due to less resolution, but reflects the fact that significant parts of the higher-degree structure average out on the millennial scale. This is also very obvious in inclination anomaly and declination. The difference between CALS3K.1 and CALS3K.2 is quite large, while on the other hand that between CALS3K.2 and CALS7K.2 is surprisingly small, considering that CALS7K.2 covers more than twice the time interval of CALS3K.2. The difference between the two 3000 year models must be attributed to the sub-

stantial differences in the data sets. The higher complexity in the radial component of CALS7K.2 reflects the relatively long time intervals during which higher-degree structure is important compared with the dipole field at the CMB during the early epochs of that model.

[43] Weak flux patches that resemble the two prominent northern hemisphere flux lobes of GUFM are present in all three millennial models in $B_{rNAD}$, but it is not obvious from the averages that the new models imply that they are stable over longer time spans than CALS3K.1 did. However, the new models' averages display a pair of positive and negative flux lobes over the Indian ocean and north of it, resembling a similar feature of GUFM. Average flux over the Pacific seems to be weaker than predicted by CALS3K.1, and is slightly weaker averaged over the past 7000 than 3000 years.

[44] The inclination anomaly average of the new 3000 year model is very weak and globally quite uniform. The stronger average anomaly over the Indian ocean in CALS7K.2 reflects the strong negative inclination anomaly observed during all the times of higher field complexity. It is puzzling that GUFM shows an even stronger average inclination anomaly centered at the same location. Looking once more at Figure 8b, however, we see that for the past 200 years the complexity has been strongly increasing and the centered dipole strength decreasing, perhaps nearing a regime where nondipole field complexity begins to show at the CMB.

## 6. Conclusions

[45] With CALS3K.2 and CALS7K.2 we have presented two new continuous global geomagnetic field models for the past 3000 and 7000 years, respectively. The major improvements over CALS3K.1 are the use of an increased, higher-resolution directional data set and intensity data, relieving the model of assumptions about axial dipole evolution. For a large fraction of the 3k year interval the models agree well with CALS3K.1 but there also are some significant differences. CALS3K.1 suggested that two historically nearly stationary flux-lobes in the northern hemisphere were transient on the millennial scale. The new models contradict this result, showing much less secular change in the northern Pacific and surrounding region.

[46] Although the spatial and temporal resolution of millennial scale models is still limited, the majority of data are fit reasonably well by our models. Improvements, however, still seem possible by studying the fit to individual data in detailed regional comparisons and building different models by a kind of jackknife technique: removing individual records from the data set to model and study the effect on the fit of the remaining records. While some regions are reliably constrained by data in the first version of a 7000 year model presented here, there remain others where the model seems to represent a compromise between "good" and "bad" data, but where we have no clear criterion for which are the more reliable.

[47] If the dating of some time series of paleomagnetic data is doubtful, a widely-used method of adjustment is the comparison of adjacent records and matching of prominent maxima and minima. Adjustments by this method become much more justified with a global model: the maxima or minima do not have to occur at exactly the same time, but at a time where it is possible to fit them in agreement with surrounding data. Any new archeomagnetic or paleomagnetic record within the past 7000 years can be used with CALS7K.2 to cross-validate dating of the data and quality of the global model in that specific region. Further improvements of millennia scale global models by including new data are anticipated. New southern hemisphere and high northern and southern latitude data would be most useful to improve our knowledge of global geomagnetic field evolution.

## Appendix A: URLs of Supplemental Material

[48] All supplemental material is stored in the EarthRef Digital Archive (ERDA). Going to http://www.earthref.org and doing a search for CALS7K or CALS3K will produce a list of our archive entries. The list of individual URLs is given below.

[49] 1. CALS7K.2, model coefficients and FORTRAN code only: http://www.earthref.org/cgi-bin/erda.cgi?n=413

[50] 2. CALS7K.2, coefficients, code, snapshots and movies centered on Pacific: http://www.earthref.org/cgi-bin/erda.cgi?n=430

[51] 3. CALS7K.2, movies centered on longitude 0: http://www.earthref.org/cgi-bin/erda.cgi?n=431

[52] 4. CALS7K.2, movies centered on north pole: http://www.earthref.org/cgi-bin/erda.cgi?n=432

[53] 5. CALS7K.1, coefficients, code, snapshots and movies centered on Pacific from the old 7000 year model: http://www.earthref.org/cgi-bin/erda.cgi?n=334

[54] 6. CALS3K.2 http://www.earthref.org/cgi-bin/erda.cgi?n=336

## Acknowledgments

[55] This work was funded in parts by NSF Grant EAR 0112290. It is an outgrowth of work completed while MK was a Feodor-Lynen fellow funded by Alexander von Humboldt Foundation at Scripps Institution of Oceanography. We thank Richard Holme and an anonymous reviewer for constructive reviews which helped to considerably improve the original manuscript. All the maps were produced by the programs "magmap" and "color" by Robert L. Parker.

## References

Brachfeld, S., G. D. Acton, Y. Guyodo, and S. K. Banerjee (2000), High-resolution paleomagnetic records from Holocene sediments from the Palmer Deep, Western Antarctic Peninsula, *Earth Planet. Sci. Let.*, *181*, 429–441.

Braginskiy, S. I., and S. P. Burlatskaya (1979), Spherical analysis of the geomagnetic field based on archeomagnetic data, *Phys. Solid Earth*, *15*, 891–895.

Constable, C. G., C. L. Johnson, and S. P. Lund (2000), Global geomagnetic field models for the past 3000 years: Transient or permanent flux lobes?, *Philos. Trans. R. Soc. London, Ser. A*, *358*, 991–1008.

Gubbins, D. (1975), Can the Earth's magnetic field be sustained by core oscillations?, *Geophys. Res. Lett.*, *2*, 409–412.

Hongre, L., G. Hulot, and A. Khokhlov (1998), An analysis of the geomagnetic field over the past 2000 years, *Phys. Earth Planet. Inter.*, *106*, 311–335.

Hulot, G., A. Khokhlov, and J. L. LeMouël (1997), Uniqueness of mainly dipolar magnetic fields recovered from directional data, *Geophys. J. Int.*, *129*, 347–354.

Jackson, A., A. R. T. Jonkers, and M. R. Walker (2000), Four centuries of geomagnetic secular variation from historical records, *Philos. Trans. R. Soc. London, Ser. A*, *358*, 957–990.

Korte, M., and C. G. Constable (2003), Continuous global geomagnetic field models for the past 3000 years, *Phys. Earth Planet. Inter.*, *140*, 73–89.

Korte, M., and C. G. Constable (2005), The geomagnetic dipole moment over the last 7000 years—New results from a global model, *Earth Planet. Sci. Lett.*, in press.

Korte, M., A. Genevey, C. G. Constable, U. Frank, and E. Schnepp (2005), Continuous geomagnetic field models for the past 7 millennia: 1. A new global data compilation, *Geochem. Geophys. Geosyst.* , *6*, Q02H15, doi:10.1029/2004GC000800.

Maus, S., H. Lühr, G. Balasis, M. Rother, and M. Mandea (2005), Introducing POMME, the POtsdam Magnetic Model of the Earth, in *Earth Observation with CHAMP: Results From Three Years in Orbit*, edited by C. Reigber et al., pp. 293–298, Springer, Berlin.

McElhinny, M. W., and W. E. Senanayake (1982), Variations in the geomagnetic dipole: I. The past 50000 years, *J. Geomagn. Geoelectr.*, *34*, 39–51.

Ohno, M., and Y. Hamano (1993), Spherical harmonic analysis of paleomagnetic secular variation curves, *Central Core Earth*, *3*, 205–212.

Sakai, H. (1980), Spherical harmonic analysis of the geomagnetic field during the last 2000 years, *Rock Magn. Paleogeophys.*, *7*, 8–15.

Yang, S., H. Odah, and J. Shaw (2000), Variations in the geomagnetic dipole moment over the last 12000 years, *Geophys. J. Int.*, *140*, 158–162.